5 Particle Physics at DESY/HERA

5.1 Electron proton collisions at 300 GeV center of mass energy: overall status of the H1–project

S. Egli, S. Hengstmann, D. Müller, M. zur Nedden, P. Robmann, F. Sefkow, P. Truöl, T. Walter, H. P. Beck (until 30. 4. 1996), V. Bickel (until 31. 3. 1997), and C. Dollfus (until 31. 8. 1996),

in collaboration with R. Eichler, C. Grab, U. Langenegger, H. Niggli, S. Passagio, D. Pitzl, L. Serbelloni, and Y. Tsipolitis, Institut für Teilchenphysik der ETH, Zürich

K. Gabathuler, R. Horisberger, and M. Wagener, Paul–Scherrer–Institut, Villigen, and 34 institutes outside Switzerland

(**H1**–Collaboration)

During its five years of operation the HERA positron-proton storage ring has delivered an integrated luminosity of 30 pb^{-1}. This sufficed for both the H1- and its rival ZEUS-collaboration to take inroads into a variety of research topics. This is evidenced by the 25 publications from the H1-collaboration alone in 1996, which are listed in the order of their appearance at the end of this section. On the other hand the luminosity is insufficient to accumulate yet large event samples for the most important processes at high momentum transfer. Nevertheless the first paper which deals with the latter region ($Q^2 > 15000$ GeV^2) has already led to a great deal of excitement, since the number of observed events (12 from neutral and 4 from charged current) exceeds that expected within the standard model description of deep inelastic lepton scattering (5 and 2, respectively). If this is not a fluctuation (an excess is also observed by the ZEUS experiment), for which the probability is less than 1 %, explanations for this observation have to be sought outside the standard model. Apart from this data, which comprises the full 1992 to 1996 sample and which we will discuss below in section 5.3.1, the analyses are based on smaller samples not including last years run, for which processing is still going on. The principal areas covered last year are:

- search for states outside the standard model [9, 10, 21];
- neutral and charged electroweak current cross sections, proton structure functions and parton densities in new domains of Bjorken x and momentum transfer Q^2 [5, 6, 23, 25, 29];
- photoproduction at high invariant masses of the photon proton system and parton densities in the photon [1, 14];
- diffractive processes and the structure of the pomeron [2, 3, 4, 24, 27];
- tests of perturbative and non-perturbative quantum chromodymanics predictions through the evolution of structure functions, and parton-fragmentation into exclusive and multijet final states [1, 4, 11, 13, 22, 26, 28];
- production of heavy quark-antiquark states [7, 8, 12].

Parameter	1992	1993	1994		1995	1996
	e^-p	e^-p	e^-p	e^+p	e^+p	e^+p
Integrated luminosity $\mathcal{L}$						
HERA produced [nb^{-1}]	–	999	938	5063	11437	14366
HERA physics [nb^{-1}]	55	880	846	4743	10403	13299
H1 taken [nb^{-1}]	30	568	532	3576	6414	8919
H1 physics [nb^{-1}]	25	528	494	3489	5745	8648
HERA efficiency [%]	–	88	90	94	91	92
H1 efficiency [%]	46	60	58	73	55	65
Average luminosity [$(\mu\text{b s})^{-1}$]	0.03	0.27	0.62	1.29	2.13	2.64
Peak luminosity [$(\mu\text{b s})^{-1}$]	0.22	1.3	2.6	4.3	5.9	8.4
Average p current [mA]	0.94	10.8	28.6	41.0	54.0	60.3
Average $e^\pm$ current [mA]	1.33	7.7	10.5	17.0	18.4	20.6
Colliding bunches	9	84	153	153	174	175
Pilot (e,p) bunches	1,1	10,6	15,17	15,17	15,6	14,6
HERA luminosity runs	132	218	116	176	304	241
Permanent H1 runs	1409	3190	1141	1816	4208	3582
Average duration [s]	973	817	1115	1620	884	1159

Table 5.1: Summary of HERA and H1 operation during the first five years. For 1994 and 1995 the runs with a shifted vertex position have been included.

Our own activities during the last year concerned as in the past the maintenance, monitoring and continuous improvement of the detector components built at Zürich for the central tracker and the first level trigger of H1 (section 5.2), and the participation in the physics analysis. We contributed in particular in the areas of photoproduction (section 5.3.3), charmed hadrons (section 5.3.4) and Bose-Einstein correlations in deep inelastic scattering (section 5.3.2).

The 1996 measuring period lasted from May to November, and accumulated 8.6 pb^{-1} of collision data (see Table 5.1). It was the second annual period after the upgrade of the H1-detector with the new backward electromagnetic calorimeter (SPACAL), a new backward drift chamber and the central silicon vertex detector. Towards the end of the 1996 run the reliability of the machine improved and HERA was producing about 1 pb^{-1} per week. To take advantage of the good performance it was decided to schedule only a very short shutdown 1996/97 without changes of the detectors and machine and continue with high efficiency. The 1997 run has already started.

5.2 Summary of activities related to the Zürich H1-components

The full **central silicon tracker (CST)** was completed and installed in the H1 experiment as reported last year during the 1995/96 shutdown. During the summer the water cooling system developed a leak and had to be switched off. Without the cooling system only one tenth of the detector could be operated simultaneously and therefore only the technical performance could be tested. Our ETH colleagues have implemented online codes for data compression and hit analysis, which were used to also obtain first results for the spatial resolution, namely 13 μm on the p-side ($r\phi$) and 25 μm on the n-side (z). The expected impact parameter resolution is however still dominated by the multiple scattering contribution from the beam pipe. Though the thinner carbon fiber reinforced plastic version built at PSI is now available, sticking to 1996 conditions also meant that the present thicker Al pipe had to be kept. In a crash effort, to which our technicians K. Bösiger and S. Steiner made extraordinary contributions, the vertex detector was removed, brought to Zürich and repaired in December 1996 and reinstalled in January 1997. It is fully operational now. The water leak unfortunately also impeded the performance of the **central inner proportional chamber (CIP)**, because for one eighth of the ϕ sectors the preamplifiers were shorted. This is also repaired now. The chamber performance otherwise showed no degradation, as witnessed with continuous monitoring of the $z-$**vertex trigger** and **big ray trigger** efficiency. These tasks were described last year in greater detail.

While the vertex detector will be important for the reconstruction of events containing charm quarks, the $z-$vertex and drift chamber track triggers are essential for triggering these events, which are characterized by low transverse energy. Since both Zürich groups are participating in analyses of these events (see section 5.3.4 below), they also play a central rôle in their collection, i. e. in the careful reoptimisation of the trigger set-up for the 96 and 97 data taking, using feedback from our own ongoing analyses. Furthermore responsibility has been taken over for the verification of the whole on- and off-line selection chain for open charm.

While during the 1995 run all rings and wires of the **central inner** $z-$**drift chamber (CIZ)** were fully efficient and stable, three of the fifteen rings, for which the wires were not replaced by new and especially cleaned ones prior to the 1995 run, developed deposits on the wires in 1996 and could no longer be operated except during cosmic test runs. The current monitoring capability of the CIZ proved again to be very important for the fine tuning of the HERA beams at the H1 interaction region.

Since October 1995 F. Sefkow acts as deputy technical coordinator of the H1-experiment.

5.3 Results from recent analyses of H1–data

The differential cross section for deep inelastic positron proton scattering, if only the neutral electromagnetic current (virtual photon-exchange) is considered, takes the following form:

$$\frac{d^2\sigma}{dx dQ^2} = \frac{2\pi\alpha^2}{xQ^4}\left[1 + (1-y)^2 2xF_1(x, q^2) + 2(1-y)F_L(x, Q^2)\right] .$$

$Q^2(\equiv -t)$ is the squared four-momentum transfer of the scattered positron and x the fraction of the proton momentum carried by the struck quark. The variable y is defined as $y = Q^2/xs$, with s being the total positron-proton center of mass energy. In a Lorentz frame where the proton is at rest, y measures the energy transfer of the positron. One of the goals of the HERA physics program is the determination of the two structure functions $F_2 = 2xF_1 + F_L$ and F_L (see e. g. [5, 23, 29]). At very high momentum transfer also the weak neutral current through Z^0-exchange has to be taken into account and a further structure function $F_3(x, Q^2)$ enters. Since both the positron and the final state hadrons marking the path of the struck quark are observed in the detector (see Figure 5.1) the kinematical variables can be reconstructed from angle and energy of either positron or hadronic jet or a combination of both. For example in term of positron quantities one finds

$$y_e = 1 - \frac{E_e(1-\cos\theta_e)}{2E_e^0} , \quad Q_e^2 = \frac{E_{T,e}^2}{1-y_e} , \quad M_e = \sqrt{sx_e} = \sqrt{\frac{Q_e^2}{y_e}} .$$

M_e is the mass of the positron-quark system, $E_{T,e}$ the transverse energy of the positron, $E_e^0 = 27.5$ GeV and θ_e is the polar scattering angle measured from the proton direction. The H1-detector [15] has a good positron energy resolution, which favors use of positron variables in particular at high momentum transfers, but important and quite accurate cross checks using the jet quantities are possible, too.

5.3.1 Deep inelastic scattering at highest momentum transfer and the standard model

The construction of the storage ring and the detectors at HERA was primarily motivated by its potential to probe the proton at very small distances ($\approx 10^{-16}$ cm) via $t-$channel exchange of highly virtual gauge bosons and to search in the $s-$channel for new particles which couple to lepton-parton pairs with masses up to $\sqrt{s} = 300$ GeV. Since the cross section decreases as Q^{-4} high luminosity is needed to study the high mass and high Q^2 region. Combining all useful runs since 1992 a total of 14.2 pb^{-1} was available for studies in this regime [25]. Selecting events with more than 25 GeV transverse positron energy, passing tight cuts on transverse momentum balance and against hard initial state positron radiation, a total of 471 candidate events are observed with $Q_e^2 > 2500$ GeV^2 and $0.1 < y_e < 0.9$, of which 443 survive further finer filtering (see [25] for details). The low y_e domain is excluded, because the resolution in M_e degrades with decreasing y_e ($\delta M_e/M_e \propto 1/y_e$). Excluding the high y values suppresses photoproduction background and also avoids the region where QED radiative effects are largest. The event selection of the charged current events uses hadron variables and leads to a sample of 31 events with $Q_h^2 > 2500$ GeV^2.

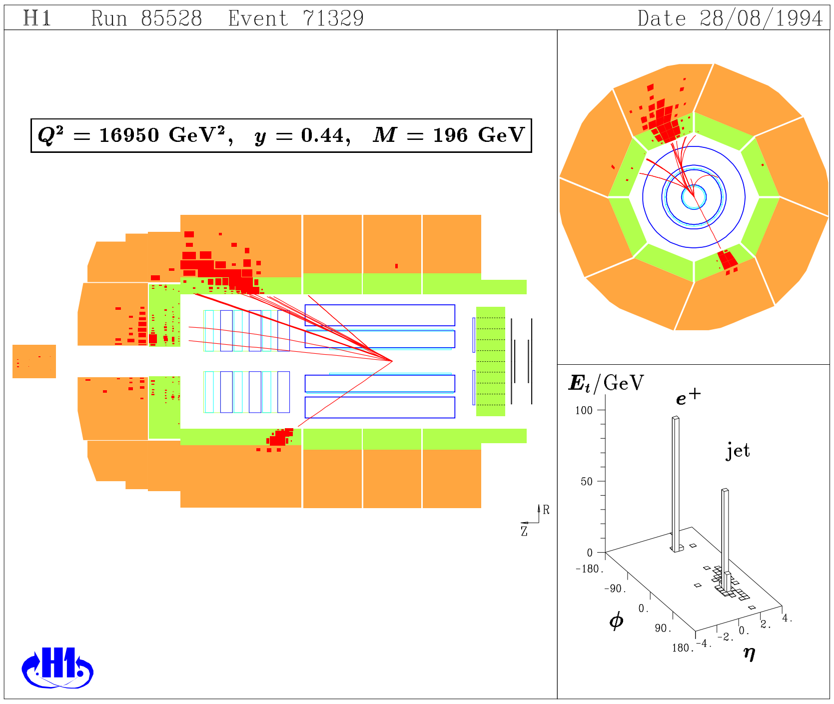

Figure 5.1: A high momentum transfer event from the neutral current sample with $M_e > 180$ GeV and $y_e > 0.4$

When these events are compared with the expectations from the standard neutral current (NC) and charged current (CC) DIS models, good agreement is obtained for $Q^2 \leq 15000\,\mathrm{GeV}^2$ for the distributions of Q^2, M_e and y_e. Figure 5.2 shows the mass distribution as an example. The models use parton distributions measured at lower energies and momentum transfers as an input and e. g. predict that 427 ± 38 events are to be expected, after full detector simulation and the same reconstruction tools and event selection criteria have been applied. At larger momentum transfer ($Q^2 > 15000\,\mathrm{GeV}^2$), 12 NC DIS candidate events are observed where 4.7 ± 0.8 are expected and 4 CC DIS candidate events are observed where 1.8 ± 0.9 are expected. One of these events is shown in Figure 5.1. The probability that the signal from standard DIS fluctuates to a number of events equal to or larger than the observed number of events is 0.006 in the NC and 0.14 in the CC case.

For the NC candidates, the excess of events is most prominent in a mass window of total width 25 GeV centered at an invariant mass $M \simeq 200$ GeV of the positron-parton system (see Figure 5.2). This mass is consistently determined using the different kinematic reconstruction methods, for which only the measured positron,

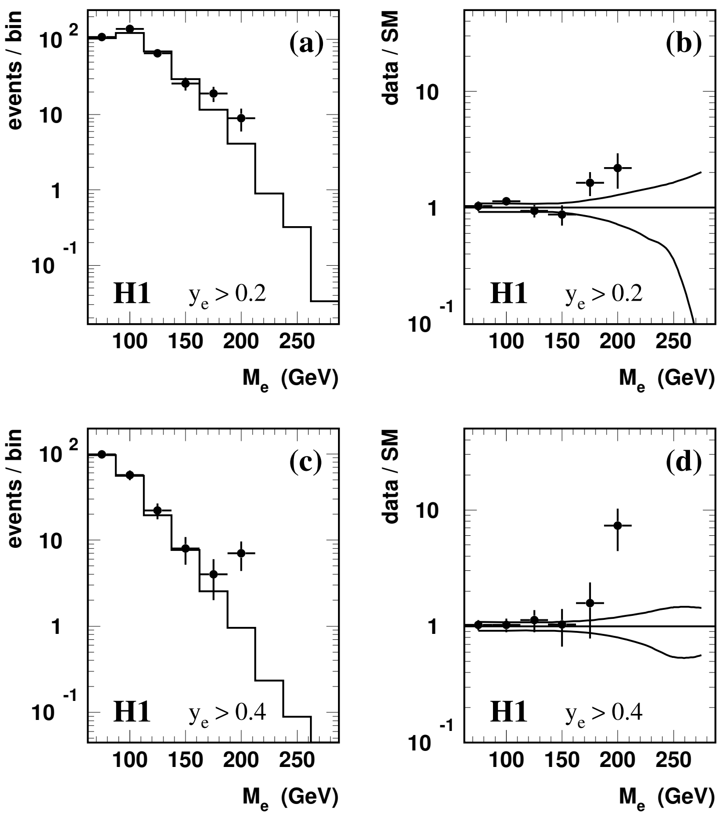

Figure 5.2: Measured distributions for the observed events (•) in the kinematical variable $M_e = \sqrt{xs}$.
a) The histogram shows the expectation from standard neutral current deep inelastic scattering models for events with $y_e > 0.2$.
b) Ratio of data to expectation for $y_e > 0.2$. The line show the one standard deviation combined systematical and statistical errors of the prediction.
c,d) as a,b), but for $y_e > 0.4$

or only the measured angles of the positron and the hadronic system, or only the four-momenta of the positron and the jet with highest E_T are used. The dominant $e +$ jet $+X$ topological feature of the events is characteristic of standard neutral current DIS processes. In a mass window of 25 GeV width with a central value of 200 GeV and for $y > 0.4$, 7 events are observed where 1.0 ± 0.2 events are expected. For this and other choices of mass windows and y thresholds, the probability to observe an excess as large as the measured one anywhere in the mass range investigated is of order 1%.

We have not been able to identify a detector effect which can account for an excess at large Q^2 or can be associated with an excess which occurs preferentially in a restricted range of M. Given the existing experimental constraints on parton density distributions at high M and lower Q^2, and given the agreement of the resulting predictions for e^+p DIS for Q^2 below $15000\,\mathrm{GeV}^2$, there is little freedom for an enhancement of the cross section at higher Q^2 by different choices for the partonic structure of the proton, by changing the strong coupling constant, or by including higher order corrections. A new mechanism would be needed to explain an enhancement of the DIS cross-section affecting mostly high Q^2 or high y values. Within the standard DIS model the only explanation of our result is therefore a statistical fluctuation. Whereas an account of the observation by introducing new physics beyond the standard model of electroweak and strong forces is kinematically possible, the signature of the observed events is identical to DIS and hence a clarification of their nature will have to come from the study of kinematic distributions with larger statistics.

5.3.2 Bose-Einstein correlations in deep inelastic electron scattering

The term Bose-Einstein correlation (BEC) normally refers to the enhanced probability for identical boson pairs to have similar momenta, which was shown to arise from the symmetrisation of the wave functions of multi-boson states. The shape of the enhancement in relative momentum space is related to the spatial dimensions of the boson source, which is why BEC have been studied in nearly every type of high-energy reaction, e. g. in e^+e^- - annihilation, in lepton nucleon (ℓN) und hadron nucleon ($\pi N, KN, NN, \overline{N}N$) scattering. Technically BEC are derived from the two-particle density $P(1,2)$ divided by the single-particle inclusive densities $P(1)$ and $P(2)$:

$$R = \frac{P(1,2)}{P(1)P(2)} \quad \rightarrow \quad R(T) = R_0(1 + \lambda \mid \tilde{\rho}(T) \mid^2) \ ,$$

The special form given above is obtained, when particles are assumed to be emitted from a set of sources distributed in space-time with a distribution $\rho(x)$, with the Fourier transform $\tilde{\rho}(T)$. R_0 is a normalisation constant and T is related to the invariant mass M of a pion pair with four-momenta p_1 and p_2: $T^2 = -(p_1 - p_2)^2 = M^2 - 4m_\pi^2$. The parameter λ is a measure of the incoherence of the source. Most experiments assume a sphere of emitters with a Gaussian density

$$\rho(x) = \rho(0)\exp(-\frac{x^2}{2r^2}) \quad \Rightarrow \quad R(T) = R_0(1 + \lambda \exp(-r^2T^2))$$

The parameter r is interpreted as the size of the production volume. In the colour-string model for the fragmentation of the partons into hadrons the length scale measured by BEC is related to the space-time separation between production points for which the momentum distributions still overlap. This distance is, in turn, related to the string tension. The model predicts an approximately exponential shape of the correlation function

$$R(T) = R_0(1 + \lambda \exp(-rT))$$

The parameter r is then expected to be independent of the total interaction energy.

Our study [8, 25] of BEC in DIS differs from previous studies of BEC in ℓN scattering not only by its tenfold higher center of mass energy. The larger range in Bjorken$-x$ and Q^2 permits a separate analysis for different bins in x, Q^2, hadronic center of mass energy W, multiplicity and for diffractive and non-diffractive events.

A sample of low Q^2 DIS events from an integrated luminosity of 1.26 pb^{-1} (1994 data) is used. The event selection used in this analysis follows closely that described in our structure function analysis [5, 23] We then form the ratio of a two-particle like-sign density $\rho_2^l(T)$ to a reference sample $\rho^{ref}(T)$, which contains no Bose-Einstein correlations.

$$R(T) = \frac{\rho_2^l(T)}{\rho^{ref}(T)}\ ,\ \rho^{ref}(T) = \ [\rho_2^u(T) \text{ or } \rho_1 \otimes \rho_1(T)]\ ,\ \rho_2^{l(u)}(T) \equiv \frac{1}{N}\frac{dn^{\pm\pm(\pm\mp)}(T)}{dT}\ .$$

N is the total number of events, $n^{\pm\pm}(T)[n^{\pm\mp}(T)]$ the number of $(++,--)[(+-)]$ pairs in the sample. For the reference sample either unlike-sign pairs or pairs obtained by mixing tracks from different events within similar kinematical classes are used. Figure 5.3 shows the full non-diffractive data sample. Table 5.2 presents some selected results for the Gaussian and the exponential parametrisation (see [8, 25] for a complete list).

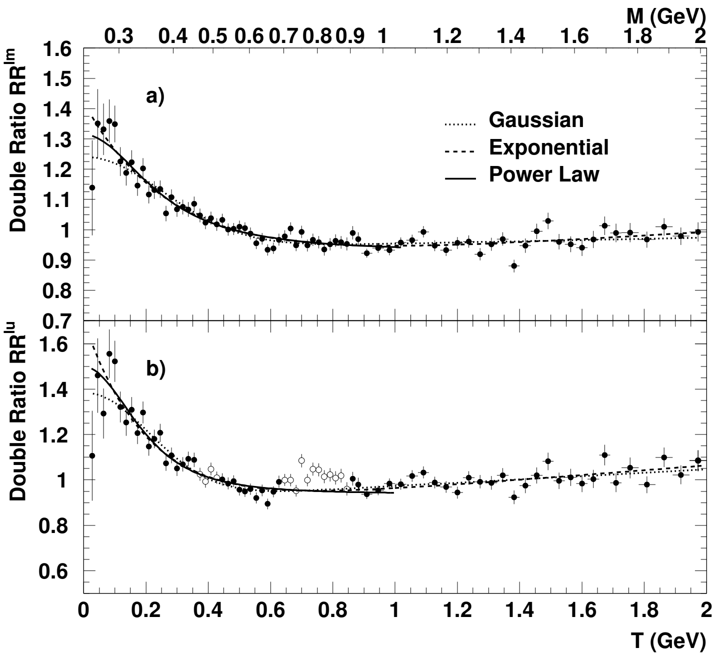

Figure 5.3: Bose-Einstein correlations in the invariant mass of like charged particle pairs: The ratio of number of like charge sign pairs to either that of unlike charge sign pairs (bottom) or uncoorrelated pairs taken from different events within similar kinematical classes (top) is plotted versus T or M. In both cases denominator and numerator are first divided by the relevant Monte Carlo generated predictions. The three curves refer to the three parametrisation of the observed enhancement at low T. The power law is not mentioned in the text.

The data provide no evidence for a statistically significant difference between the BEC parameters in predominantly non-diffractive and diffractive DIS interactions.

This observation of similar BEC effects supports the idea that the basic fragmentation mechanism is similar. The same holds for those kinematical subsets for which the results have not been shown. In qualitative agreement with hadron collider data we also observe a dependence of r and λ on the multiplicity, or on the particle density per interval of pseudorapidity computed from the corrected multiplicity [13]. With our track selection criteria we are sensitive to an interval in the $\gamma^* p$ center of mass system $\Delta\eta^* = 3.2$ $(1.1 < \eta^* < 4.3)$.

Data set	r (fm)	λ
non-diffractive	$0.54 \pm 0.03\ ^{+0.03}_{-0.02}$	$0.32 \pm 0.02\ ^{+0.06}_{-0.09}$
diffractive	$0.49 \pm 0.06\ ^{+0.02}_{-0.03}$	$0.46 \pm 0.08\ ^{+0.15}_{-0.08}$
$4 \leq n < 7$ $(4.9 \pm 1.1^\dagger)$	0.42 ± 0.05	0.37 ± 0.05
$7 \leq n < 12$ $(8.2 \pm 1.6^\dagger)$	0.58 ± 0.05	0.31 ± 0.03
$n \geq 12$ $(13.6 \pm 2.4^\dagger)$	0.81 ± 0.12	0.42 ± 0.07
Exponential	$0.68 \pm 0.11\ ^{+0.09}_{-0.06}$	$0.64 \pm 0.06\ ^{+0.17}_{-0.16}$

Table 5.2: Summary of experimental results extracted using the Gaussian prametrisation; top: comparison between diffractive and non-diffractive data; middle: comparison of subsets of different multiplicity ($^\dagger \equiv$ corrected multiplicity and spread for each bin). Bottom: fits to the non-diffractive data set using the exponential parametrisation. All data sets use the event mixed reference sample. Where given the first error is statistical, the second is systematic.

Table 5.3 summarises the Gaussian fit results from other high-energy experiments for comparison with the present analysis. The fact that the data from $\ell N-$scattering are independent of the energy, and furthermore agree with those from e^+e^--annihilation at various center of mass energies (with the exception of the MARK II - data), seems to lend support to the string model interpretation, where hadronisation is seen as a universal phenomenon and the measured spatial dimensions reflect mainly the constant string tension.

5.3.3 Photoproduction

Besides DIS at HERA also reactions of high energy photons with the proton can be studied in a new kinematic regime extending the available total center of mass energy by an order of magnitude compared to fixed target experiments. This allows to confront the perturbative QCD predictions and the predictions of Regge- and Pomeron models with the data in a kinematic regime which so far has not been accessible.

During the last year the research concentrated on the topics of diffractive dissociation in photoproduction [24], the structure of the virtual photon, and on the

Experiment		event-mixed $\rho_1 \otimes \rho_1(T)$		$\sqrt{s}$ or W
		r(fm)	λ	[GeV]
DELPHI	e^+e^-	0.47±0.03	0.24±0.02	91
ALEPH		0.52±0.02	0.30±0.01	91
AMY		0.58±0.06±0.02	0.39±0.04±0.03	58
MARK II		0.97±0.10±0.05	0.27±0.04±0.02	29
TPC		0.65±0.04±0.05	0.50±0.04	29
EMC	μp	0.46±0.03	0.73±0.06	23
E665	μp	0.39±0.02	0.35±0.02	30
BBCNC	νN	0.64±0.04	0.46±0.03	10-28
H1	ep	0.54±0.03±0.03	0.32±0.02±0.09	300

Table 5.3: Gaussian fit results from other experiments with $\sqrt{s} \geq 29$ GeV, or $W \geq 23$ GeV.

determination of an effective parton distribution in the photon. The latter subject is discussed now in more detail.

Perturbative QCD predicts a unique characteristic for the probability $f_{q/\gamma}$ of finding a quark with the energy fraction x_γ in the photon: the probability depends directly on x_γ , but also on the factorization scale μ_f at which the quark of the photon is probed, thus leading to a logarithmic scale dependence. This scale dependence is due to the so called anomalous component of the photon, which is absent for parton distributions in hadrons.

The analysis is based on the measurement of double differential di-jet cross section in photoproduction processes from data corresponding to an integrated luminosity of $2\,\mathrm{pb}^{-1}$. The photoproduction events were selected by requiring that the scattered electron disappears in the beam pipe, undetected in the central detector (so-called untagged events). The photon virtuality is therefore restricted to $Q^2 < 4\,\mathrm{GeV}^2$. The jets were found using a cone algorithm with cone size $R = 0.7$ and jet pseudo-rapidities in the range $-0.5 < \eta^{jet} < 2.5$. The jet transverse energy had to be above $E_T^{jet} > 8\,\mathrm{GeV}$. The rapidity difference between the two jets was required to be below $\Delta\eta < 1$ in order to integrate over a small interval of the parton scattering angle: $\tanh(\Delta\eta/2) = \cos\theta^*$. The corrections for detector effects were calculated using an unfolding procedure.

The cross section is measured both as a function of the parton fractional energy x_γ^{jets} and the transverse energy scale E_T of the jets. In particular the scale dependence is reflected in the dependence of the cross section on E_T. Here x_γ^{jets} is defined by the two jets with the highest E_T^{jet} in the event:

$$x_\gamma^{jets} = \frac{E_T^{jet1} e^{-\eta^{jet1}} + E_T^{jet2} e^{-\eta^{jet2}}}{2 y_{jb} E_e} \tag{5.1}$$

The measurements are compared to leading order (LO) QCD calculations, which include both direct and resolved photon processes (see Figure 5.4). The calculation gives an overall satisfactory description of the data, but falls low at large x_γ^{jets} and high E_T. In these kinematical regions modifications to the input parton distribution of the photon are needed.

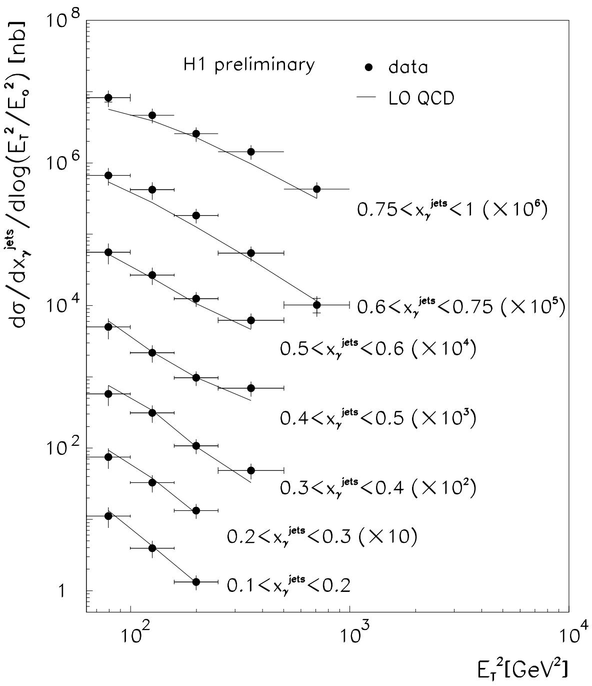

Figure 5.4: The measured differential di-jet ep cross section is shown as a function of the logarithm of the squared jet transverse energy $\log{(E_T^2/E_\circ^2)}$ in bins of the reconstructed parton fractional energy x_γ^{jets} (full circles, $E_\circ^2 = 1$ GeV^2). The cross section is integrated over the photon virtuality $Q^2 < 4\,\mathrm{GeV}^2$, the relative photon energy $0.2 < y < 0.83$ and the jet pseudo-rapidities in the HERA laboratory frame $-0.5 < \eta^{jet1,2} < 2.5$ and $\Delta\eta^{jets} < 1$. The data are compared to a LO QCD calculation of the PYTHIA generator with multiple interactions using the GRV-LO parton distribution functions for the proton and the photon (full curves).

In a second step one can use this data to extract an *effective* parton distribution [$R1$] of the photon, which sums the contributions from quark and gluon density functions in the photon weighted by different colour factors. To get the effective parton distribution of the photon the di-jet data were corrected with the same unfolding procedure as used above, but now the data were corrected for underlying event energy effects, for fragmentation and parton shower effects to the leading order parton level (see Figure 5.5).

The effective parton distribution of the photon increases with the scale p_T^2 as expected from the anomalous component of the photon splitting into quark antiquark pairs [$R2$]. The increase appears slightly steeper than expected from the GRV-LO effective parton distribution. In the GRV distribution the contribution $\frac{9}{4}g$ drops with x_γ and is around 20% at $0.4 < x_\gamma < 0.7$. In this x_γ region the increase is dominated by the quark content of the photon. The data clearly disfavour a purely hadronic parton distribution of the photon, but are compatible with the QCD prediction of

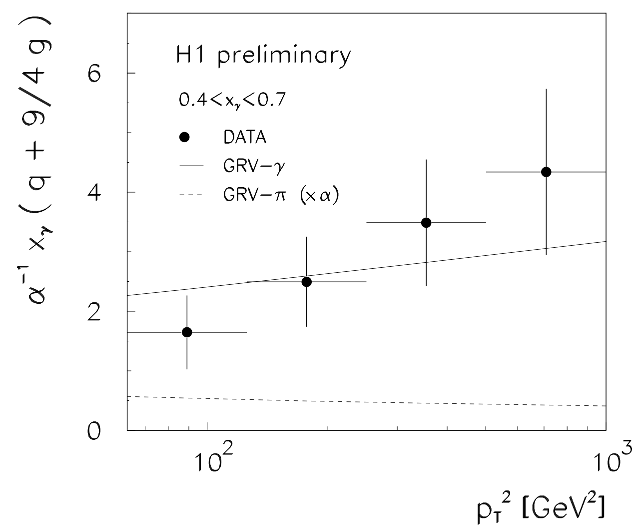

Figure 5.5: The extracted leading order effective parton distribution of the photon $f_{i/\gamma}^{eff} = q + \frac{9}{4}g$ is shown as a function of the squared parton transverse momentum p_T^2 in bins of the fractional parton energy x_γ. The data are compared to the effective parton distribution of the photon (full curve) and the pion (dashed curve, omitting $1/\alpha$) calculated with the GRV-LO parton distribution functions.

the anomalous component in the photon.

[R1] B.L. Combridge and C.J. Maxwell, Nucl. Phys. **B239** (1984), 429.
[R2] E. Witten, Nucl. Phys. **B120** (1977), 189.

5.3.4 Photo- and Electroproduction of Charm Quarks

Charm quark production accounts for one quarter of the total DIS cross section at HERA [12, 19]. Understanding heavy flavour production is therefore essential for a complete description of the proton structure. In the framework of QCD, the production proceeds via the photon gluon fusion mechanism where a photon emitted from the incoming electron interacts with a gluon in the proton by forming a quark-anti-quark pair. Therefore, studying charm events also offers the classical way towards a determination of the gluon density in the proton. Studies in that direction are pursued using events where either a J/Ψ or a D meson (open charm, discussed here) has been detected, in photoproduction and in DIS. The cleanest signal for open charm is obtained in the decay chain $D^{*+}{\to}D^0\pi^+$, $D^0{\to}K^-\pi^+$ and forms the basis of the results selected here.

First measurements of differential charm photoproduction cross sections, as functions of transverse momentum and rapidity, have been published by H1 using the data collected in 1994 [8]. In photoproduction, also so-called resolved processes contribute, where the photon fluctuates into a hadronic state and a parton from that state interacts with the proton. The interpretation of the data thus also depends on the poorly known photon structure, to an extent that is subject to current theoretical debate. Experimental errors are still large, and more precise data are highly desirable to distinguish between models. An update of this analysis with twofold statistics, using 95 data (Figure 5.6), has already been shown [30], the analysis of the 1996 data promises at least another factor of two.

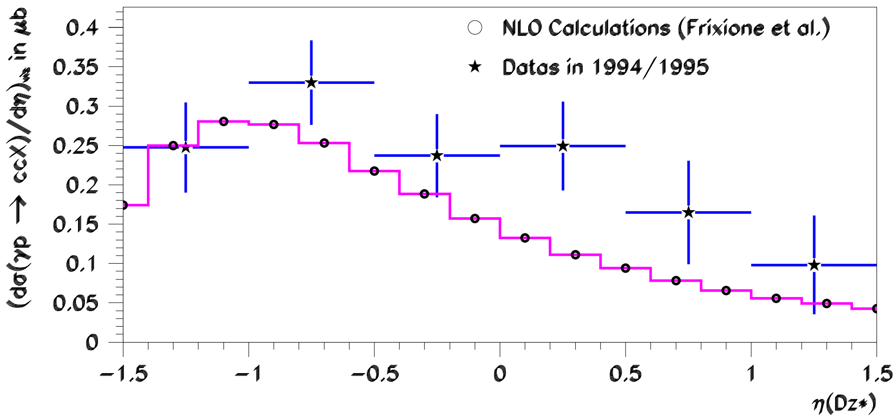

Figure 5.6: Differential charm cross section versus rapidity in tagged photoproduction, for transverse momenta $p_t(D^*) > 2.5$ GeV/c. The QCD prediction (in NLO) uses the parametrisations MRS G and GRV-HO for the parton densities in the proton and photon, respectively.

In DIS, the resolved component is absent, and one has a clearer picture. The charm contribution to the proton structure function, $F_2^{c\bar{c}}(x_{Bj}, Q^2)$, is almost entirely determined by the gluon content in the proton, and has been measured by H1 [12]. It is possible to go even further and make use of the additional kinematic information from the reconstructed charm tag, in order to reconstruct the momentum fraction x_g of the incoming gluon and thus arrive at a direct measurement of the density function $g(x_g)$. We have shown [31] a first measurement of the differential charm cross section as a function of $x_g(had)$, which was reconstructed from the D^* meson and the scattered positron (Figure 5.7). Again the analysis of the three times larger 1996 sample is underway. QCD predictions in next-to-leading order (NLO) for such distributions at the level of observable hadrons have recently become available. The programs have been adapted to the H1 analysis, results are overlaid in Figure 5.7 and indicate that a steeper gluon distribution like the MRS G parametrization is preferred by the data. The QCD program also yields the correlations with the 'true' x_g which can be used to unfold the gluon density from the measured spectrum.

[1] Jets and Energy Flow in Photon-Proton Collisions at HERA, S. Aid et al., Z. Phys. **C70** (1996), 17.
[2] Elastic Photoproduction of ρ^0 Mesons at HERA, S. Aid et al., Nucl. Phys. **B463** (1996), 3.
[3] Elastic Electroproduction of ρ^0 and J/Ψ Mesons at Large Q^2 at HERA, S. Aid et al., Nucl. Phys. **B468** (1996), 3.
[4] Energy Flow in the Hadronic Final State of Diffractive and Non-Diffractive Deep-Inelastic Scattering at HERA, S. Aid et al., Z. Phys. **C70** (1996), 609.

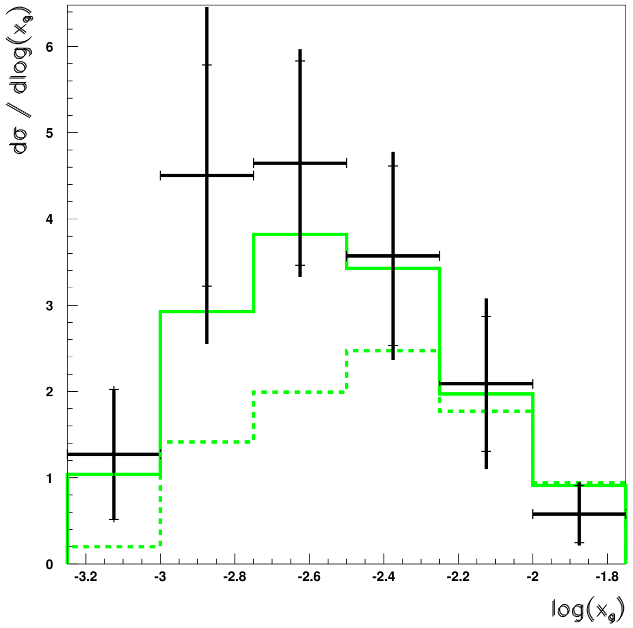

Figure 5.7: Differential charm cross section in DIS, for $Q^2 > 2$ (GeV/c)^2. versus parton momentum fraction $x_g(had)$, as reconstructed from the D^* meson and the scattered electron. The histograms are QCD calculations in NLO, using the MRS G (full line) and MRS D^0 (dashed) parton density parametrizations for the proton.

[5] A Measurement and QCD Analysis of the Proton Structure Function $F_2(x, Q^2)$ at HERA, S. Aid et al., Nucl. Phys. **B470** (1996), 3.

[6] Measurement of the Q^2 Dependence of the Charged and Neutral Current Cross Sections in ep Scattering at HERA. S. Aid et al., Phys. Lett. **B379** (1996), 319.

[7] Elastic and Inelastic Photoproduction of J/Ψ Mesons at HERA, S. Aid et al., Nucl. Phys. **B472** (1996), 3.

[8] Photoproduction of $D^{*\pm}$ Mesons in Electron-Proton Collisions at HERA, S. Aid et al., Nucl. Phys. **B472** (1996), 32.

[9] A Search for Squarks of Rp violating SUSY at HERA, S. Aid et al., Z. Phys. **C71** (1996), 211.

[10] Search for Selectrons and Squarks at HERA, S. Aid et al., Phys. Lett. **B380** (1996), 461.

[11] Strangeness Production in Deep Inelastic Positron-Proton Scattering at HERA, S. Aid et al., Nucl. Phys. **B480** (1996), 3.

[12] Inclusive D^0 and $D^{*\pm}$ Production in Deep Inelastic ep Scattering at HERA, C. Adloff et al., Z. Phys. **C72** (1996), 593.

[13] Charged Particle Multiplicities in Deep Inelastic Scattering at HERA, S. Aid et al., Z. Phys. **C72** (1996), 573.

[14] Scale Influence of the Energy Dependence of Photon-Proton Cross Sections, S. Aid et al., Phys. Lett. **B392** (1997) 234.

[15] The H1 Detector at HERA, I. Abt et al., Nucl. Instr. Meth. **A386** (1997), 310 (part I); ibid. 348 (part II).

[16] Photon Structure and Charmed Meson Production at HERA, S. Egli, Proc. 31rd Rencontres de Moriond: '96 QCD and High Energy Hadronic Interactions, Les Arcs, France (March 1996), ed. J. Trân Thanh Vân (Ed. Frontieres, Gif-sur-Yvette 1996), p. 363.

[17] Measurement of the Total Photoproduction Cross Section at the Electron Proton Collider HERA at $W_{\gamma p}$ of 200 GeV, H. P. Beck, Thesis Universität Zürich (1996).
[18] Bose-Einstein Correlations in Deep Inelastic Scattering at HERA, C. Dollfus, Thesis Universität Zürich (1996).
[19] Heavy Flavour production at HERA, F. Sefkow, Proc. Les Rencontres de Physique de la Vallée d'Aoste: Results and Perspectives in Particle Physics, La Thuile, Italy (March 1996), Ed. M. Greco, Frascati Physics Series Vol. V (1996), p. 539.
[20] Neutral and Charged Current Processes in Positron Proton Collisions at HERA, P. Truöl, PANIC 96, XIV. Int. Conf. on Particles and Nuclei, College of William and Mary, Williamsburg, Virginia, USA (May 1996), Proc. eds. C. E. Carlson and J. J. Domingo (World Scientific, Singapore 1997), p. 46.
[21] Search for Excited Fermions with the H1 Detector, S. Aid et al., Nucl. Phys. **B483** (1997), 44.
[22] Measurement of Charged Particle Transverse Momentum Spectra in Deep Inelastic Scattering, S. Aid et al., Nucl. Phys. **B485** (1997), 3.
[23] Determination of the Longitudinal Proton Structure Function $F_L(x, Q^2)$ at Low x, C. Adloff et al., Phys. Lett. **B393** (1996), 452.
[24] Diffraction Dissociation in Photoproduction at HERA, C. Adloff et al., DESY 97 – 009, Z. Phys. **C** (1997), in print.
[25] Observation of Events at very High Q^2 in ep collisions at HERA, C. Adloff et al., DESY 97 – 024, Z. Phys. **C** (1997), in print.
[26] Bose-Einstein Correlations in Deep Inelastic ep Scattering at HERA, C. Adloff et al., to be submitted to Z. Phys. **C**.
[27] Electroproduction of ρ^0 Mesons with Proton Diffractive Dissociation and of Elastic Φ Mesons at HERA, C. Adloff et al., to be submitted to Nucl. Phys. **B**.
[28] Photoproduction of K^0 and Λ at HERA and a Comparison to Deep Inelastic Scattering, C. Adloff et al., to be submitted to Nucl. Phys. **B**.
[29] A Measurement of the Proton Structure Function $F_2(x, Q^2)$ at Low x and Low Q^2 at HERA, DESY 97 – 042, C. Adloff et al., submitted to Nucl. Phys. **B**.
[30] Messung differenzieller Wirkungsquerschnitte für $c\bar{c}$ - Ereignisse in Photoproduktion bei HERA, M. zur Nedden, 61. Physikertagung DPG, Universität München.
[31] Untersuchungen zur Gluon-Dichte im Proton mit D^*-Ereignissen bei HERA, D. Müller, 61. Physikertagung DPG, Universität München.

5.4 Microstrip gas chamber development for the HERA-B experiment

A. Maag, P. Robmann, S. Steiner, P. Truöl, and T. Walter,
in collaboration with
Universität Heidelberg and Universität Siegen

We joined the HERA-B collaboration in 1995 and decided to assist in the construction of the inner tracking detector and in the manufacture of microstrip gas chambers (MSGC's). We regarded our involvement in this experiment as important in the preparation for the CMS project at the LHC (see section 5). The MSCG's planned for use in the HERA-B experiment are quite similar to those under discussion for the CMS-experiment and hence can serve as a realistic large scale prototype.

MSGC's are position sensitive particle detectors, where thin metallic strips of typically 10 μm width every 300 μm on a glass surface serve as anodes, which are interspersed by typically 150 μm wide cathode structures. Such a glass substrate then is separated from a grounded plane by an active gap of typically 3 mm width. Microstrip gas chambers were chosen for the inner tracking system of the HERA-B detector, because large fluxes up to 10^6 mm^{-2}s^{-1} at small radii near the beam pipe demand a very high granularity.

In the collaborative effort with the Heidelberg and Siegen Universities we accepted to be responsible for the design of the masks, and the supervision of production and quality control of the substrates for all modules, the manufacture of the complete modules within the magnet and their mechanical supports and lastly for beam tests in PSI pion beams. It is these three areas, where our work concentrated last year.

5.4.1 Infrastructure

Figure 5.8 shows a photograph of the clean flow box, which was installed last year in our laboratory, and which houses the scanning optical microscope. If a substrate is to be inspected, it can be mounted on an accurate measuring and positioning device under the microscope. The coordinates can be recorded by a computer, which also controls the movement to a new position. In this way possible faults can be detected, if necessary photographed, classified and recorded. This system allows magnifications between a factor of 50 and 1000, covers an object area of up to 40$\times$40 cm^2, is capable of a digital position recording accuracy of 1 μm, and is mounted on a marble plate supported with shock absorbers. The system integration, computer control and coordinate readout was developed by us, while the microscope, clean box, positioning device and coordinate display was acquired commercially [1]. The quality control of a a large numbers of chambers with this system is quite time consuming. Substrates with too many anode breaks can be eliminated quicker using an electrical method, which we have developed [2]. Large RF-signals ($\approx$ 30 V, 30 -

Figure 5.8: The scanning optical microscope with automatic position recording in the newly installed clean room.

100 kHz) are fed to copper strip, which extends across one end of all anodes and sits right below the substrate. The height of the pickup signal measured for each anode changes for those with a fault. The whole set up is housed in a small clean box to protect the plate, the anodes are contacted via small spring loaded pins and the signal multiplexed for the readout. Figure 5.9 shows the signal dependence when the contact is moved along an anode with a break.

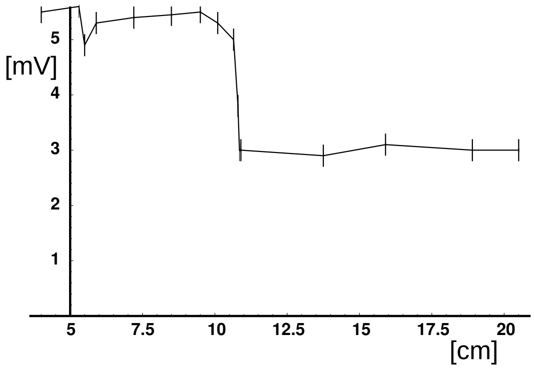

Figure 5.9: Signal recorded by the receiver in the anode tester, if the emitter is moved across a break in an anode structure of a microstrip gas chamber. This test was made with the large full size MSGC prototype for HERA-B (Layout UZHHERA1)

We have listed in Table 5.4 the different masks, which have been laid out in Zürich and from which chambers have been produced at IMT (Greifensee) first on clean DESAG 263 glass substrates (ion conducting, surface resistivity $> 10^{16}$ Ω/square) and later on diamond coated glas substrates (chemical vapour deposition, 8×10^{14} Ω/square). The full size prototype (UZHHERA1) is one of the largest MSGC ever built. The glass thickness is however 550 μm for this design as opposed to the 300 μm used for all others and desired for the final chambers. For the electrodes different materials were used, namely chromium, gold and rhodium coated Cr, and aluminum. Some of the special tools needed to handle the substrates in the production process at IMT, in particular for the largest sizes, were produced in our shops, too.

type, special features	substrate size [cm^2]	anode width [μm]	cathode width [μm]	pitch [μm]	number of anodes
UZHMSGC1					
design tests	12.7×12.7	8/10/12	172/170/168	300	16/16/16
fixed cathode		10-6/12-8/14-10	172/170/168	300	16/16/16
var. gap		6-10/8-12/10-14	172/170/168	300	16/16/16
fixed gap		10-6/12-8/14-10	174-166	300	16/16/16
var. cathode		6-10/8-12/10-14	174-166	300	16/16/16
var. gap/cathode		10	190/210/230	300	16/16/16
UZHMSGC2					
var. gaps	12.7×12.7	10	130/150/170	300	101/101/101
UZHHERA1					
full size prot.	27.5×24.1	10	170	300	767
UZHMSGC3 Cr/Au anode Ti cathode	12.7×12.7	10	170	300	101/101/101

Table 5.4: Overview of MSGC masks produced in Zürich.

5.4.2 Chamber tests

In Zürich the chamber test stand with readout chain, gas system and trigger counters was only recently brought into operation. All tests reported below were therefore made in Heidelberg and Siegen with sources and X-ray tubes (irradiation and high intensity tests), with the exception of measurements in the PSI pion beam (April 1996) and in the HERA-B hall (autumn 1996) [3]. Primarily the 12.7×12.7 cm^2 plates were used with the UZHMSGC2 electrode layout (normally 0.5 μm Au on Ti backing) with a drift gap of 3.3 mm and a 50/50% argon/dimethylether gas mixture. For the readout 4×4 anodes within 16 commonly supplied cathodes were combined to one group. Despite the microscopically poor quality of the anode borders (see picture in last years annual report) the chambers operated satisfactorily at gain factors around 3000, with and without diamond coating. The coated plates however demonstrated superior ageing characteristics and made them the prime candidate for the high rates expected at HERA-B. During the PSI test it was however discovered, that chamber breakdowns occured at the intolerably high rate of a few sparks per hour. Visual inspection of the chamber after the test indicated a close correlation of the number of anode defects and holes in cathodes (see Figure 5.10) with the number of sparks, most noteably for the gold plated anode, where often large pieces were found missing. This phenomenum was subsequently confirmed by adding a radon admixture to the chamber gas as arising from heavily ionizing beam particles or spallation fragments passing the chamber gap initiating a sustained electron avalanche. In the HERA environment the spark rate was also found to be too high for a safe operation over longer periods. Pure Cr anodes were found to be less affected, but the specific resistance of such anodes prevents their use in large chambers, because of the signal reduction. Alternatives to gold like rhodium were also unsuccesfully investigated, after the techniques to produce such layers were developed by IMT.

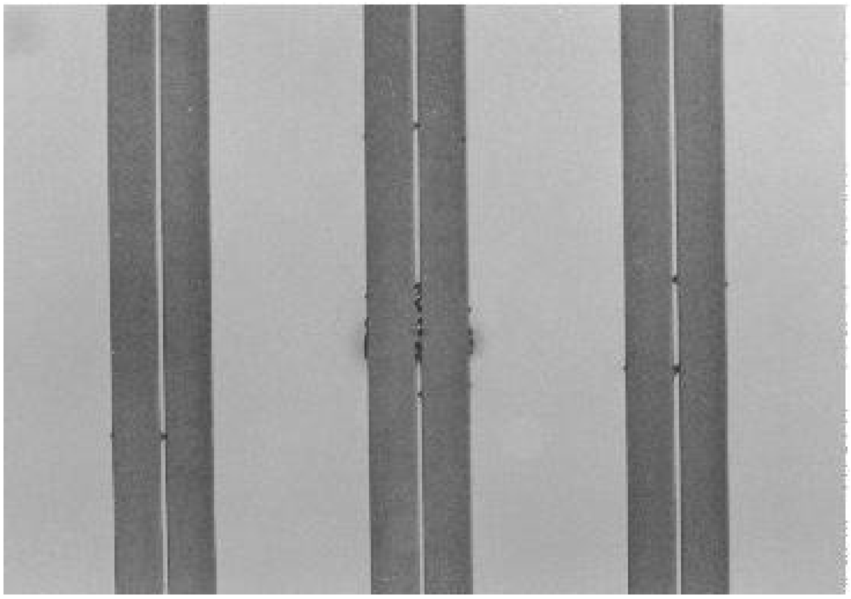

Figure 5.10: Observed damages on a microstrip gas chamber substrate with chromium electrodes after sparking induced by strongly ionizing particles.

As a consequence of these tests (which were also confirmed independently by other groups) we had to reach the unfortunate conclusion in December 1996, that a MSGC-prototype, which will survive several years of HERA-B running, has not been found. Low resistivity anodes are needed to get a fast signals and in practice only gold seems acceptable, which is damaged by every single spark. One therefore needs to build chambers which can not spark at any serious level. Ideas which have been put forward and which are followed up to remedy the problems are

i) hybrid chambers with high resistivity cathodes and low resistivity anodes on coated glass (this prevents discharges and still allows for fast signals of sufficient amplitude),

ii) Cr electrodes on coated Kapton with gold pickup electrodes on the backplane

(Cr electrodes were found to sustain higher spark rates and the pickup line assures good signals),

iii) thicker gold anodes (raises anode survival rate in case of sparking and keeps signal shape),

iv) the gas electron multiplier (GEM) technique [4], or

v) the advanced passivation [5].

For the first two alternatives, which are followed up by our Heidelberg and Siegen colleagues, respectively masks and frames have been produced in Zürich, and essais at IMT have been made, but no results are available yet. The advanced passivation technique covers the electrodes at their borders with an insulating polymer of a few μm width to reduce electric field concentration. The tests made in Heidelberg with three chambers received from Pisa-CERN group (CMS) proved this solution unviable for the HERA-B inner tracker, too.

In the GEM technique a thin mesh made from a double sided metal clad polymer is added in front of the microstrip plate. The mesh has conical holes of 50 μm diameter with a 140 μm pitch. A moderate voltage difference across the mesh produces an electrical field and consequent electron multiplication, which in turn allows to operate the subsequent MSGC at lower gain and in a safer mode. A modified MSGC with a GEM foil obtained from the CERN group was tested in Heidelberg at the tenfold HERA-B rate with X-rays and alpha particles without observation of sparks. This chamber has been installed recently in the HERA-B beam.

We made successful tests in collaboration with local companies (IMT, Greifensee; Flühmann, Dübendorf) to produce Au anodes on Cr backing using galvanic techniques. Figure 5.11 demonstrates, that the electrochemical deposition leads to higher edge quality of the Au strips as compared to the lift-off technique used so far. Furthermore Au layers with more then 3 μm thickness were reached on 12.7×12.7 cm^2 substrates without faults. The assembly of a complete MSGC is in preparation.

The difficulties encountered with MSGC's forced us also to consider alternative solutions. Scintillating fibres promise to be the most quickly realisable replacement for the MSGC's of the inner tracker of the HERA-B experiment. Apart from the considerably higher cost and increased amount of material within the spectrometer the main problems here are the marginal light output for thin detector layers, radiation damage, light attenuation in the long clear fibres leading to the photomultipliers, shielding of the latter against magnetic field. Since the beginning of the year a test program was started in collaboration with DESY Zeuthen and Hamburg to find the right fibres, measure the light output, irradiate prototype module, instal a detector sheet into the HERA-B beam, i. e. to seriously evaluate this alternative. We have investigated how such a detector could be mounted inside the HERA-B magnet and will assist in its production, should the comparison between the MSGC and the fibre solution favour the latter. The inner tracker group aims at a decision for one or the other solution by May 1997.

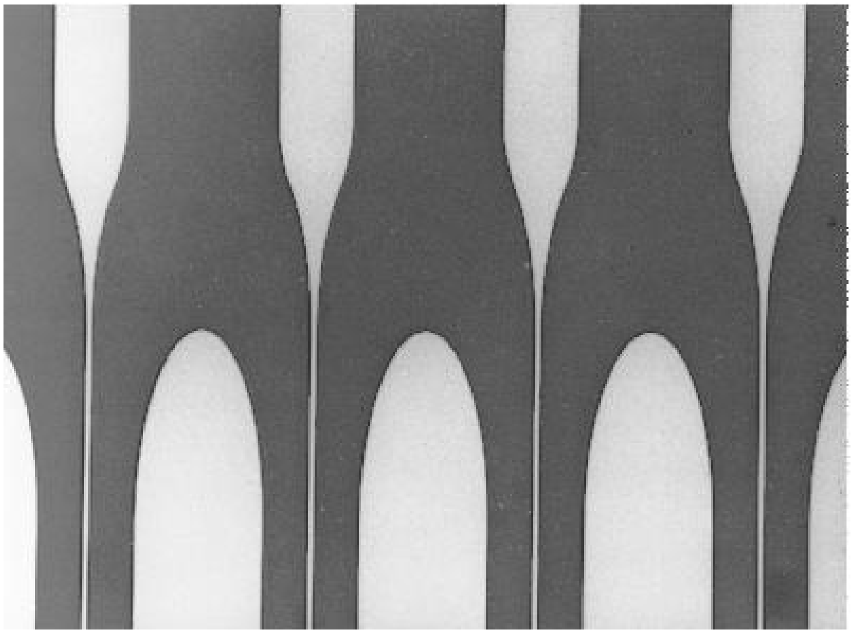

Figure 5.11: End zone of a MSGC plate, which was produced with galvanic coating

[1] Computer controlled scanning of large microstrip gas chamber substrates using an optical microscope, P. Robmann, S. Steiner and T. Walter, UZH-MSGC-Report 97-01.
[2] Electrical method for detecting anode breaks on microstrip gas chamber substrates, A. Maag, Diploma Thesis, University of Zürich (1997), UZH-MSGC-Report 97-02.
[3] Untersuchungen von Prototypen der Mikrostreifen-Gaskammern des inneren Spurkammersystems des HERAB Experiments, S. Visbeck, Diploma Thesis, University of Heidelberg (1996). See also T, Hott, Thesis, University of Heidelberg (1997).
[4] R. Bouclier et al., CERN preprints PPE/96-177; PPE/97-032; F. Sauli, Nucl. Instr. Meth. B (1997), in print.
[5] Short summary on tests with advanced passivated chambers at Heidelberg, B. Schmidt (2-97) (available at: http//www.physi.uni-heidelberg.de/groups/he_desy/MSGC_Info.html).